Fabrication of Particle-Stacking Microporous Metal Using Laser Powder Bed Fusion

Jinyong Qiu , Xiaoqiang Xu , Yanlong Wu * , Xu Chen * , Yaxiong Liu

Posted Date: 5 February 2024

doi: 10.20944/preprints202402.0218.v1

Keywords: Laser powder bed fusion; Microporous metal; Particle-stacking

Article

Fabrication of Particle-Stacking Microporous Metal Using Laser Powder Bed Fusion

Jinyong Qiu [1,2], Xiaoqiang Xu [1,2], Xu Chen [1,2], Yaxiong Liu [1,2,*] and Yanlong Wu [1,2,3,*]

[1] School of Mechatronic Engineering and Automation, Foshan University, Foshan 528000, China
[2] Ji Hua Laboratory, 528200, Foshan, China
[3] School of Mechanical and Automotive Engineering, South China University of Technology, Guangzhou 510640, China
* Correspondence: liuyx@jihualab.com (Yaxiong Liu), wyl098531@163.com (Yanlong Wu)

Abstract: Laser powder bed fusion can fabricate porous structure through lattices, but it remains a challenge to prepare micropores (<100 μm) with a specific pore distribution. Here, microporous 316L was fabricated by controlling the behavior of melting and solidification of particles with the rapid heating and cooling of laser. The results showed laser energy density was not a determining factor for porosity and micropore formation, except for the single factor. High-speed scanning mode required higher laser power disordered the pore distribution, while low-speed scanning with low laser impact on the stacking particles formed organized pores. Hatch distance greatly affected the distribution and size of pores. The pore distribution in XY plane showed organized and homogenous with channeled pores mainly interconnected along the laser scanning tracks, whereas in Z direction showing a relatively disordered distribution mainly linked along the layered direction. The microporous 316L displayed a pore size of 10 - 50 μm (D50) and 50 - 100 μm (D90) with a high-percentage size distribution in 1 - 10 μm, a controllable porosity of 17.06% - 45.33% and a good yield strength of 79.44 - 318.42 MPa superior to the lattice porous 316L with 250.00 MPa at the similar porosity.

Keywords: laser powder bed fusion; microporous metal; particle-stacking

1. Introduction

Porous metallic materials due to the existence of pores, gives them dual attributes of being structural and functional [1,2], which has attracted much attention in recent years. With many extraordinary characteristics of low relative density, large specific surface area, light weight, sound insulation and energy absorption, porous metals are widely applied in the fields of structural lightweight [3,4], medical implant [5–7], filtration and separation [8,9], sound absorption and noise reduction [10–12], heat exchange [13–15] and battery catalysis [16,17]. Therein, porous structure with channeled pores and pore size less than 100 μm plays a particularly important role in the physical and chemical performances for the excellent connectivity and high specific surface area of micropores. For instance, interconnected micropores in catalysis with specific channels, allowing media such as gases or liquids to pass through, can increase the effective diffusion rate of ion and gas media, and improve the electrochemical reaction rate with a large specific surface area [18].

Lots of traditional techniques have provided many routes to prepare metallic porous structure by foaming, templating, sponge replicating and dealloying [19–21]. Unfortunately, these traditional techniques often have the shortcomings of being complex processes, having long lead-time, with high comprehensive cost or requiring advanced equipment. Hence, it is necessary to find a simple, efficient and rapid way to fabricate the microporous metallic materials. Additive manufacturing (also known as 3D printing technology), as an advanced manufacturing technology, provides a new alternative pathway to build the porous metals rapidly. Laser powder bed fusion (LPBF) [22] as a typical mature commercial technique of additive manufacturing, enables the free fabrication of components with

 doi:10.20944/preprints202402.0218.v1

single-step formation. Consequently, LPBF has become popular and reliable to fabricate complex metallic components, including porous metals with lattices. With various lattice structures, porous metals with all kinds of porous structures nowadays have been successfully manufactured, as reported in the literatures [23–27]. Lattice porous structures, however, are mostly limited to the millimeter-sized scale with low specific surface area [23–28], which hinders the further application of LPBF for porous structure manufacture. It is still a challenge to fabricate the micropores less than 100 μm and meanwhile design the pores with the desired configuration via LPBF printing. Some researchers have attempted to fabricate these micropores through controlling the densification process of metals by laser energy density. Won Rae Kim [29] et al attempted to prepare microporous Ti under low-energy-density process conditions below that required for the complete melting of Ti. Zhenjun Li [30] et al prepared porous Ti6Al4V with some micropores by changing its laser hatch spacing for a low laser energy density and investigated relationship between the porosity and tensile strength. However, they did not reveal the relationship between the pore distribution of locations in structure and the laser energy, nor did they study the effect of laser parameters on the pore size and size distribution, which is very important for formation of micropores and the customization of pore configuration. Not to mention fabricate the interconnected pores with regular controllable pore distribution by controlling a specific output of laser energy.

In this work, we focused on the fabrication of channeled micropores with organized controllable pore distribution via using LPBF parameters for specific laser energy to control the melting, overlapping and stacking of metal particles. As the typical material used in LPBF printing, 316L stainless steel was selected. The effect of the printing parameters on porosity, pore distribution of locations in structure, pore size and size distribution were investigated. The compressive performance of the microporous structure was also given, compared with a lattice porous 316L. This work provides a simple and effective way to prepare the microporous metal structures via using LPBF, which may be significantly instructive and the possible solution for customization of pore configuration, even the gradient microporous structures.

2. Materials and Methods

2.1. Fabrication of Particle-Stacking Microporous 316L

The raw powder used in this experiment was 316L stainless steel powder (15 - 53 μm, Jiangsu Vilory Advanced Materials Technology Co., Ltd.) with a good sphericity (as shown in Fig 1a), enabling a good flowability (≤ 18 s 50^{-1} g) and a high packing density (≥4.10 g·cm^{-3}). The printer used in this experiment was AmPro SP100 system (Suzhou AmPro Ltd., China) with an Nd: YAG fiber laser of wavelength 1.06 μm, laser power up to 200 W, laser scanning speed of up to 2000 mm·s^{-1} and layer thickness of 10 - 50 μm. The microporous cubic 316L specimens (10 mm × 10 mm × 10 mm) were built on the same material substrate without any preheats and three of them were fabricated at each parameter set. The detailed printing process was: first, a layer of microporous structure with a certain degree of "particle-to-particle" overlapping was formed after a specific laser scanning, where the metal particles went through rapid melting and solidification as the result of the superfast heating and cooling of the laser with a high laser-induced heating temperature up to 10^5 K and a rapid cooling rate up to $10^{6–7}$ K·s^{-1} [31]. Next, these layered porous structures were stacked layer upon layer and then formed a bulk porous metallic material with the desired micropores. As shown in Figure 2, the pore distribution in structure, pore size and size distribution have close association with the laser energy, which could be determined by the main printing parameters (e.g., laser power, laser scanning speed, hatch distance and layer thickness). The whole printing was conducted under high purity nitrogen with the oxygen content below 100 ppm in the printing chamber to protect 316L metal powder from oxidation.

The LPBF-printed particle-stacking porous samples of 316L were shown in Figure 1b, which shows that there are no obvious visible cracks and defects can be found on these microporous samples with flat surfaces.

 doi:10.20944/preprints202402.0218.v1

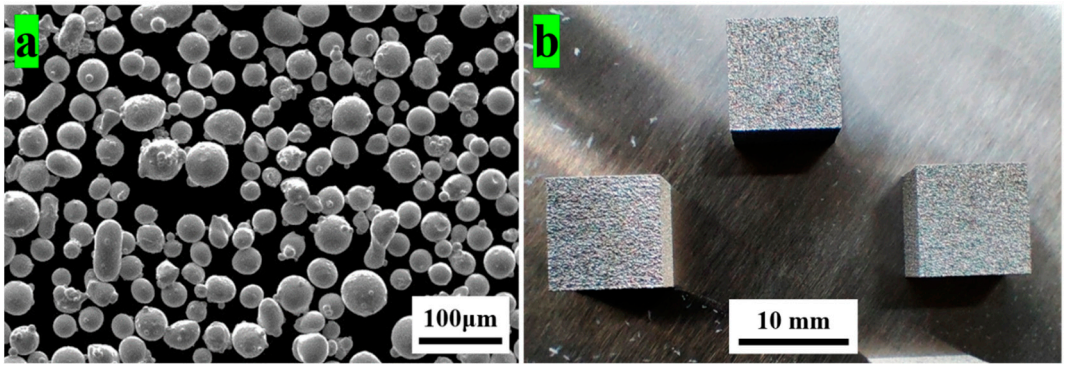

Figure 1. 316L raw powders and LPBF-fabricated microporous 316L. (a) SEM image of 316L spherical powders and (b) representative LPBF-fabricated particle-stacking samples.

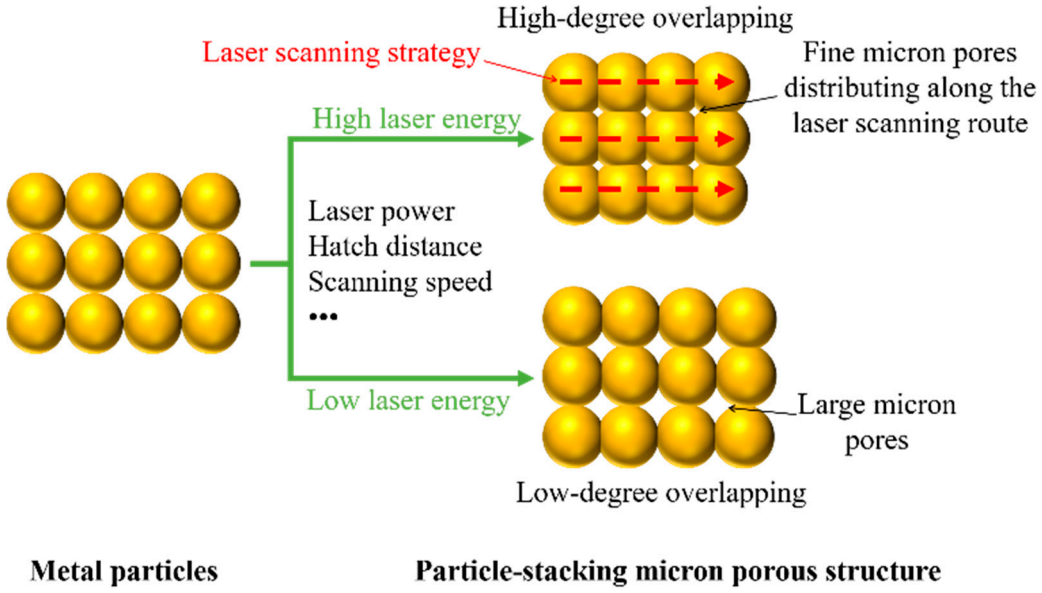

Figure 2. Schematic diagram of microporous particle-stacking porous structure via laser powder bed fusion.

2.2. Characterization

To measure the porosity, three LPBF-printed samples of every parameter set were first mechanically polished to 1 μm roughness on all sides. The polished samples were then precisely weighed as the bulk weight (W_{bulk}) and their bulk volume (V_{bulk}) was computed with the three-dimensional size. Then the ρ_v defined as volume density (i.e., relative density) could be calculated with the quotient of bulk weight divided by bulk volume, as shown in formula (1). The porosity ($P_{porosity}$) was obtained by the following formulas [32]:

$$\rho_v = \frac{W_{bulk}}{V_{bulk}} \quad (1)$$

$$P_{porosity} = \frac{V_{pores}}{V_{bulk}} * 100\% = \left(1 - \frac{\rho_v}{\rho_{theory}}\right) * 100\% \quad (2)$$

Where ρ_v, $P_{porosity}$, V_{bulk}, W_{bulk}, and ρ_{theory} represents volume density (or relative density), porosity, bulk volume, bulk weight, and theoretical density, respectively.

Morphological observations on the cross-sections of microporous 316L were characterized by optical microscope (OLYMPUS GX53) and the morphology of 316L powders was observed by scanning electron microscope (SEM, NOVA NANOSEM 430). Pore size and size distributions were measured by the post-processing software packages ImageJ analysis software (NIH, Bethesda, MD).

 doi:10.20944/preprints202402.0218.v1

Three-dimensional microstructure was determined by computed tomography (CT) image conducted with using a 3D X-Ray microscope, Xradia 620 Versa (ZEISS, Germany) with a 0.5 μm resolution in the range of 3 × 3 × 3 mm^3.

The quasi-static compressive properties of the microporous 316L samples with different porosities were tested by using an electronic universal mechanical tester (CMT4303, MTS, USA) at a constant load rate of 1.0 mm min^{-1} (strain rate of ~ 0.003 s^{-1}). The compression force was applied in the direction perpendicular to the printing plane. The compressive yield strength was calculated according to the stress-strain curves.

3. Results and Discussion

3.1. Effect of Laser Power and Laser Energy Density on Microporous Structure

Figure 3 shows the effect of laser power and the corresponding energy density on the porosity of LPBF-fabricated microporous 316L at two modes of "high-speed scanning of the equipment ultimate speed of 2000 mm·s^{-1} ("HS" mode for short hereafter)" and "low-speed of 600 mm·s^{-1} ("LS" mode for short" hereafter). The porosity of these samples at two modes showed first sharply decreasing from an abnormal high point then gradually levelling off. The porosity of "HS" mode and "LS" mode changed from the abnormal high value of 71.05% down to 17.06% and 75.82% down to 23.43%, respectively. Both modes at the low laser power (i.e., 70 w for "HS" mode and 40 w for "LS" mode) clearly showed a bad quality with some visible defects of abnormal coarse holes, having the relatively abnormal high porosity of 71.05% for "HS" and 75.82% for "LS", which indicated that the laser energy at this low-power condition was not available for the formation of the stacking porous structure. Once upon this power ("HS" went over 70 w and "LS" over 40 w), both modes formed good-quality porous samples without any visible defects.

Aside from the abnormal porosities, it is obvious that the porosities at the two modes could be linearly fitted, as shown with the red dashed line in Figure 3. The fitting equations were also given alongside, which could be utilized as an instructive basis to fabricate a microporous structure with a desired porosity. The slope of the curve of "HS" mode (value = 0.35) was lower than that of "LS" mode (value = 0.56), which indicated that it had a wider operating laser power range for designing a desired porosity since applying the high-speed scanning mode. The reason might be that the high-speed scanning with a lower energy density could refine the distribution accuracy of laser energy on particles, which thus allowed the laser energy was about to be controlled and distributed more precisely for each particle.

It is very interesting that all the points of laser energy density of "HS" mode are lower than that of "LS", but not all the porosity of "HS" is higher. For instance, the porosity at 50 w (with laser energy density of 34.72 J·mm^{-3}) of "LS" mode is 28.20%, higher than that of "HS" at 120 w (with porosity of 25.74% and energy density of 25.00 J·mm^{-3}) and 130 w (with porosity of 23.43% and energy density of 27.08 J·mm^{-3}). In particular, though the energy density of "LS" at 40 w still had 27.78 J·mm^{-3}, higher than that of "HS" at 120 w and 130 w, it still showed an abnormal porosity of 75.82% with visible abnormal holes, indicating the failed fabrication of microporous structure. On the contrary, "HS" presented normal porosities until the laser energy density is down to 14.58 J·mm^{-3} at 70 w, which demonstrated the condition of high energy density did not necessarily obtain a better formation than that of low energy density. According to the definition and calculation formula of laser energy density, there are several variable factors, such as power, scanning speed, hatch distance and layer thickness. In the case of single variable factor, laser energy density can definitely and directly determine the formation of porous structure and the porosity. But in the case of two-factor changes, it does not, just like this in this case, which illustrated that energy density was not the determining indicator, except under the condition of single factor.

 doi:10.20944/preprints202402.0218.v1

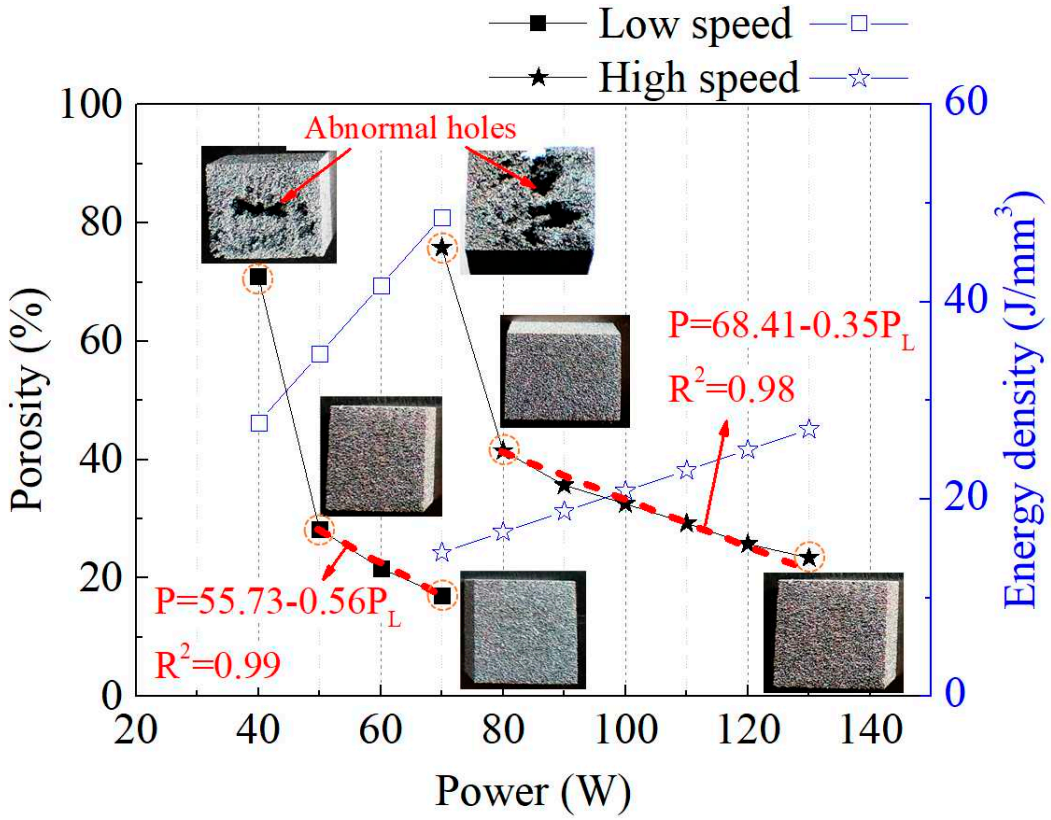

Figure 3. Porosity of microporous 316L samples printed by LPBF as a function of the different laser power at two scanning modes of low laser scanning speed (600 mm·s-1) and high laser scanning speed (2000 mm·s-1): Red dash lines are the fitted lines with the fitted equations to the corresponding data, where P and PL represent porosity and laser power, respectively.

To analyze the effect of laser power on the porous structure, morphology observation on the corresponding cross-sectional microstructure of the as-printed microporous 316L was carried out, as shown in Figure 4. It could be found that the particle-stacking microporous structure showed irregular pore morphology, formed by the interaction of "particle-to-particle" overlapping and stacking. This was quite different from the pores with a spherical morphology caused by some bubbles remained in the molten pools, because the rapid-cooling rate of the laser prevented them from escaping out of the molten metal liquid before totally solidification [33]. On the overlapping joints between particles, typical sintered necks could be obviously observed, as shown by the yellow mark in the magnified image in Figure 4a. The pores of "HS" mode distributed randomly, especially its low-power sample, containing a lot of localized large interconnected pores. There were lots of isolated small-sized spherical particles within the pores could be found, which indicates that they were most likely caused by splash deposits. Within the sintered strut, it formed lots of spherical pores with much smaller size as the result of rapid solidification under the rapid scanning speed. In its high-power sample, the number of localized large pores clearly reduced, but the high power led to excessive overlapping or even the disappearance of pores in some zone, as verified with the disappearing pores and disappeared pores as marked in the magnification in Figure 4b.

On the contrary, the samples of "LS" showed homogenous distribution of pores along the uniform molten tracks with a good particle melting and overlapping. There were few localized large pores and less isolated spherical particles as that in the "HS". Particularly, no such small-sized spherical pores were observed within the strut. The main reason may be that a large temperature gradient, strong laser impact pressure and Marangoni flow [34–36] would be caused by the high laser power at "HS" mode. These brought serious impacts on the 316L particles, leading to much more movements or splashes of particles, which finally disorders the stacking pores. However, low-speed scanning mode provided more time for the escaping out of the molten metal liquid before

 doi:10.20944/preprints202402.0218.v1

solidification. Meanwhile, low-speed scanning with a low impact pressure of laser would thus be beneficial for melting the particles mildly and keep a good stacking state of particles on bed, which could fabricate a structure with orderly distributed pores along the laser scanning.

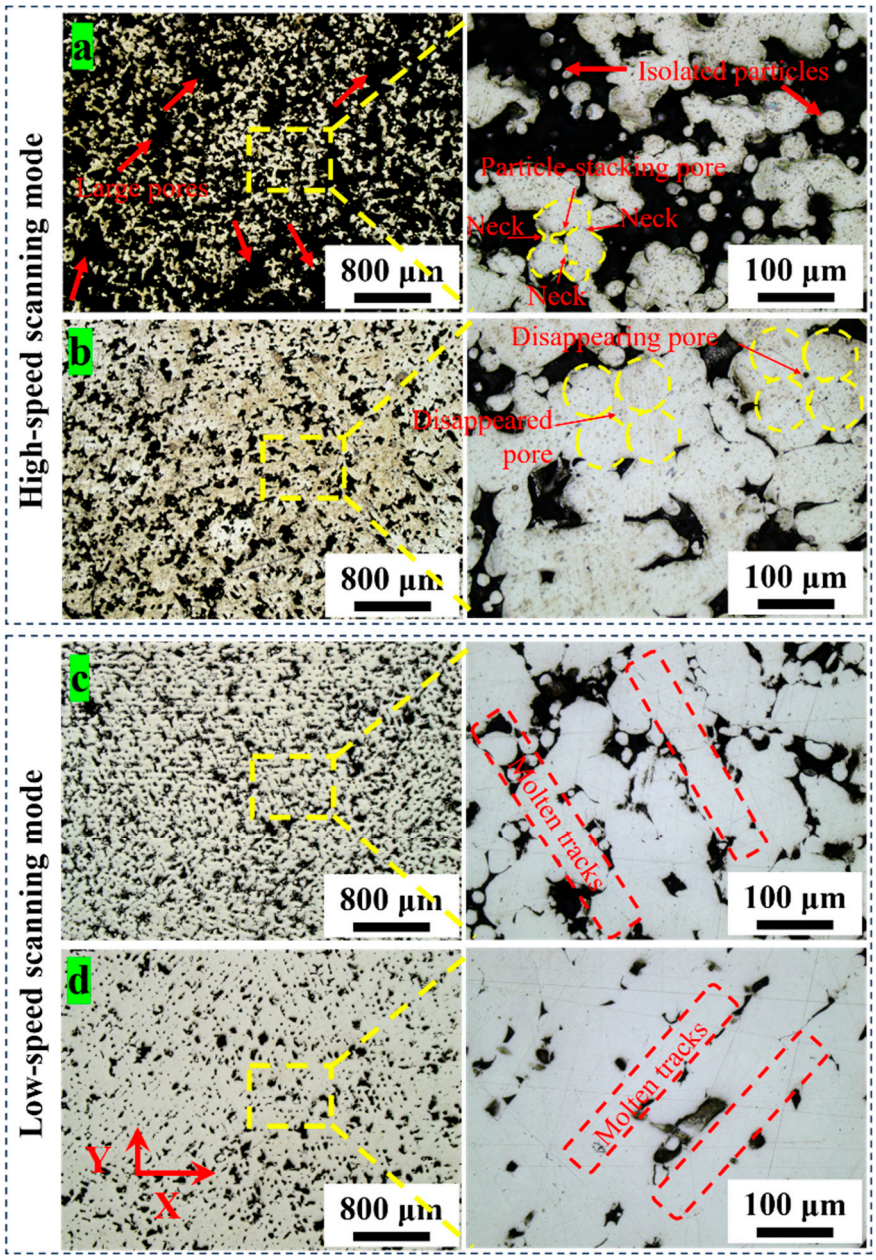

Figure 4. Cross-sectional micrographs of particle-stacking microporous 316L samples fabricated with different laser power at two modes of high-speed scanning and low-speed scanning: (a) 80 w and (b)130 w at high scanning speed of 2000 mm·s-1, (c) 50 w and (d) 70 w at low speed scanning of 600 mm·s-1.

To quantify the relationship of laser power and porous structure, the arithmetic mean particle size, median pore size and size distribution were statistically undertaken, as shown in Table 1 and Figure 5, respectively. It could be clearly seen that almost all of the arithmetic diameters of pores built with particle-stacking were less than 100 μm. The mean particle sizes were larger than the median pore size of D50 for including the whole pores. With the increase of laser power, both pore sizes decrease transparently, in agree with the porosity. As seen from the size distribution, all the sample showed a semi-gaussian distribution concentrated to the left side, with a near-horizontal variation at 1 - 10 μm, indicating a high percentage of small-sized pores in the size distribution of 1 - 10 μm. Lager than 10 μm, it began to drop slowly. The pore size at “LS” mode decreased significantly from (D50)

 doi:10.20944/preprints202402.0218.v1

30.00 μm to 14.75 μm and (D90) 85.50 μm to 73.75 μm, with the increase of laser power from 50 w to 70 w. While the pore size at "HS" mode showed 50.75 μm (D50) to 14.00 μm and 135.75 μm (D90) to 72.75 μm, as the laser power increased from 80 w to 130 w. In particular, the sample of "HS" mode with low laser power at 80 w showed much larger pore size with obvious wider pore size distribution compared to the other samples. There were even some large pores over approximately 500 μm, which corresponded to its massive localized large pores, due to the low laser energy density supplied by the laser, as shown in Figure 4a.

Table 1. Pore size corresponding to the cross-sectional porous structure in Figure 4.

Sample	LS-50 w	LS-70 w	HS-80 w	HS-130 w
Mean(μm)	40.61	21.83	63.88	29.23
D50(μm)	30.00	14.75	50.75	14.00
D90(μm)	85.50	73.75	135.75	72.75
Porosity%	28.20	17.06	41.50	23.42

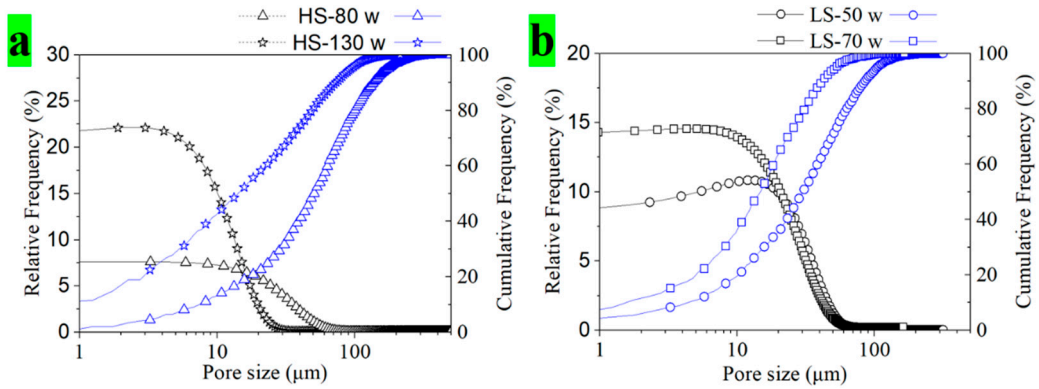

Figure 5. Pore size distribution of microporous 316L samples fabricated with different laser power at two modes of high-speed scanning and low-speed scanning: (a) high scanning speed of 2000 mm·s-1 and (b) low speed scanning of 600 mm·s-1.

3.2. Effect of Laser Scanning Speed on Microporous Structure

Based on "LS" mode with a more ideal pore distribution as previously discussed, we attempted to raise the porosity and meanwhile further optimize the pore structure by appropriately increasing laser scanning speed. Figure 6 shows the porosity of microporous 316L fabricated with the fixed power at 60 w and the laser scanning speeds varied from 600 mm·s^{-1} to 1400 mm·s^{-1} at 200 mm·s^{-1} intervals. With the increase of laser scanning speeds, the porosity increased from 27.03% to 72.11%, much higher than that of "LS". This is because increasing the scanning speed would reduce the contact time of the laser and particles at the constant laser energy, which would indirectly decrease the amount of energy received by the particles at per unit time. It is worth noting that the porosity increased 57.08% when the laser scanning speed increased from 1200 mm·s^{-1} to 1400 mm·s^{-1}. However, the porosity only increased 17.31% when the laser scanning speed increased from 1000 mm·s^{-1} to 1200 mm·s^{-1} with the same increment. This corresponded to that the macroscopic defects of abnormal holes (see the red marking in Figure 6) generated due to some un-melted particles with insufficient laser energy when laser scanning speed increased to 1400 mm·s^{-1}, which indicated that the particle-stacking porous structure was not able to be normally formed beyond this speed.

 doi:10.20944/preprints202402.0218.v1

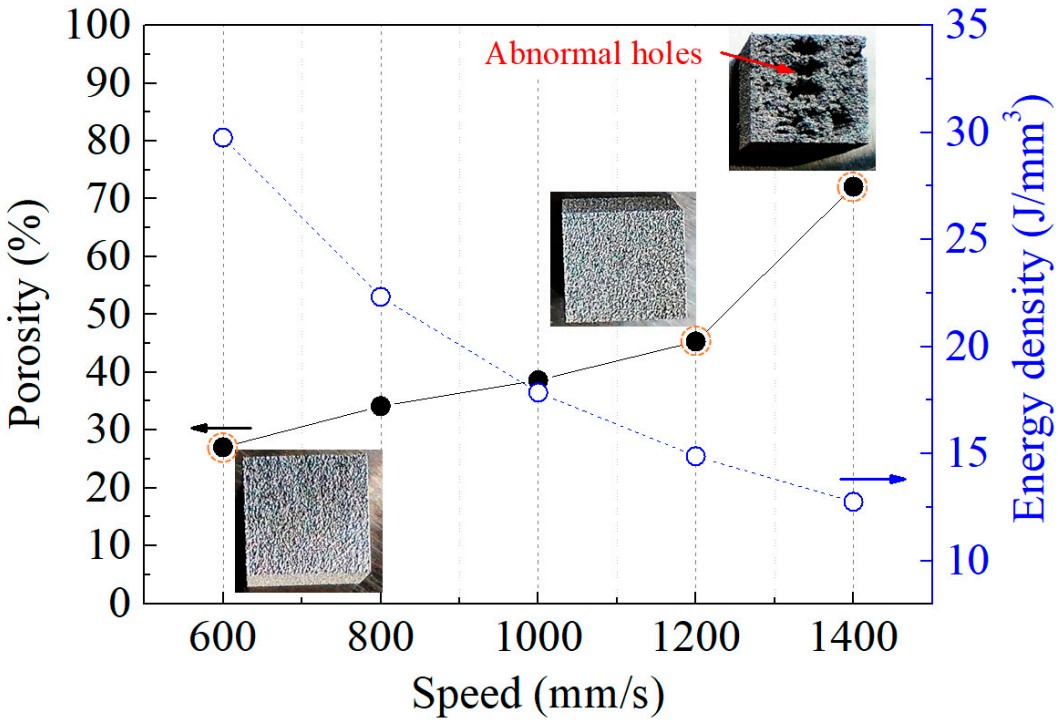

Figure 6. Porosity of microporous 316L printed by LPBF as a function of the laser scanning speed.

Figure 7 shows the cross-sectional morphologies of the microstructures at different laser scanning speeds. As expected, it could be found that the pores with irregular morphology distributed homogenously and orderly along the scanning tracks when using the laser scanning speed under 1200 mm·s^{-1}. In comparison with the sample printed with the scanning speed of 1400 mm·s^{-1} (with macroscopic defects of abnormal holes as seen in Figure 6), although no macroscopic defects were found on surface of the sample at the laser scanning speed of 1200 mm·s^{-1}, it had already formed lots of abnormal localized large pores at the size of about 500 μm and massive isolated um-melted particles within the pores. This indicated that the pores could keep small size with well distribution when the scanning speed is below 1000 mm·s^{-1}.

 doi:10.20944/preprints202402.0218.v1

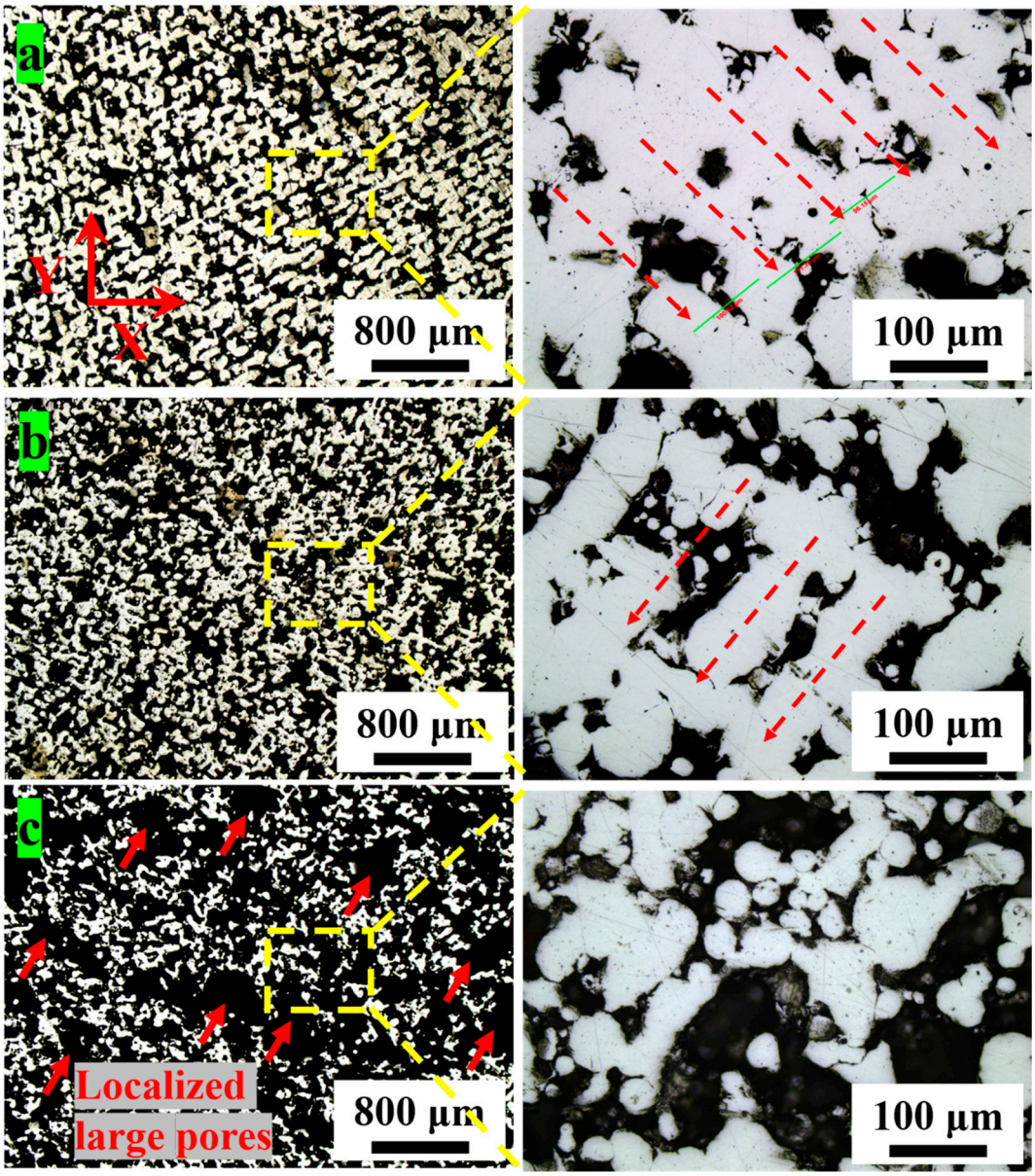

Figure 7. Cross-sectional pore structure of microporous 316L samples fabricated with different laser scanning speed: (a) 800 mm·s^{-1}, (b) 1000 mm·s^{-1}, (c) 1200 mm·s^{-1}.

Table 2 shows the pore size corresponding to the cross-sectional porous structure at different laser scanning speeds as mentioned above. With the increase of laser scanning speeds, the pore size increased from 28.00 μm (D50) to 55.75 μm and 84.25 μm (D90) to 159.25 μm. The pore size of D50 increased 38.51% from 40.25 μm to 55.75 μm as the scanning speed increasing form 1000 mm·s^{-1} to 1200 mm·s^{-1}. However, it could be observed that a relatively large increment in the pore size of D90 increased 68.07% from 94.75 μm to 159.25 μm. This corresponded to the microstructure with massive localized large pores at the scanning speed of 1200 mm·s^{-1}, as shown in Figure 7c.

Figure 8 gives the size distribution at different laser scanning speeds. Likewise, the pore size distributions showed the same semi-gaussian distribution concentrated to left side, indicating that the porous structures had high percentage of fine pores as well. With the increase of scanning speed, the percentage of pores distributed in the small size (<100 μm) gradually reduced and on the other side the large-sized pores continuously appeared, even some localized large pores over 500 μm.

 doi:10.20944/preprints202402.0218.v1

Table 2. Pore size corresponding to the cross-sectional porous structure in Figure 7.

Sample	Mean(μm)	D50(μm)	D90(μm)	Porosity%
800 mm·s^{-1}	40.82	28.00	84.25	34.15
1000 mm·s^{-1}	51.18	40.25	94.75	38.64
1200 mm·s^{-1}	74.65	55.75	159.25	45.33

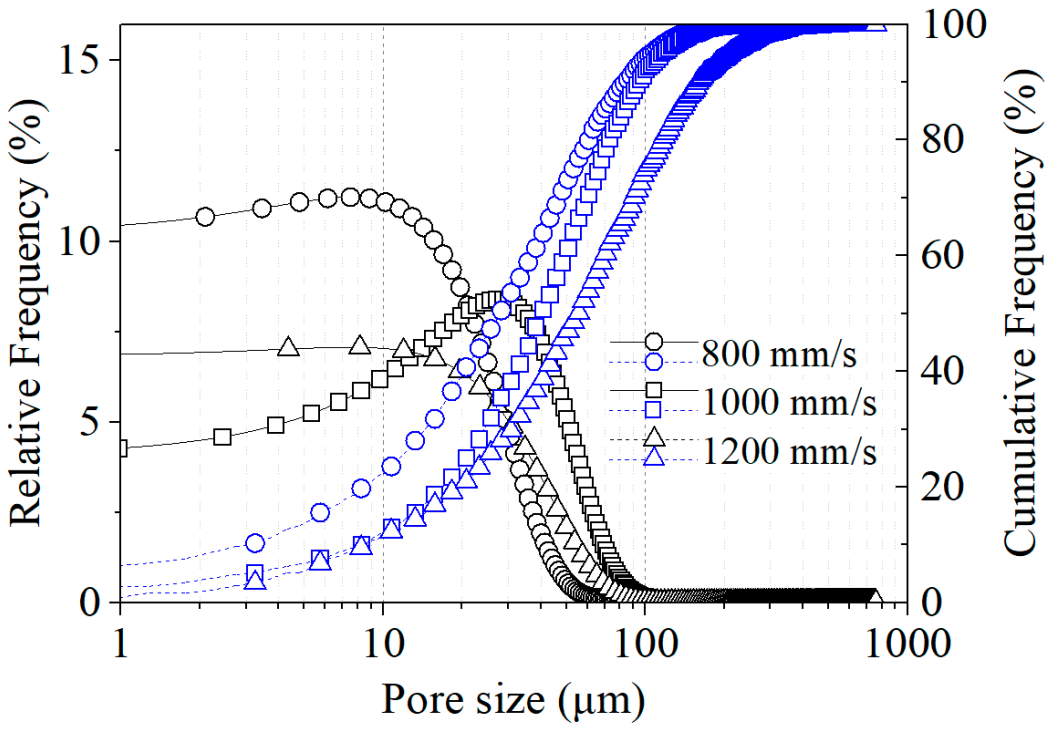

Figure 8. Pore size distribution of microporous 316L samples fabricated with different laser scanning speed.

3.3. Effect of Hatch Distance (HD) and Layer Thickness (LT) on Microporous Structure

Figure 9 shows the porosity of microporous 316L printed with different hatch distance at the scanning speed of 600 mm·s^{-1}, the layer thickness of 30 μm and 42 μm, respectively. As the hatch distance increased, the porosity of the samples fabricated with LT of 30 μm showed a tendency of first rapidly increasing and then gradually levelling off. However, the porosity of the samples with LT of 42 μm went extremely high at the HD of 0.14 mm. These might be related to the grow up of pores with the increasing hatch distance. On one hand, the increase of HD decreased the laser energy distribution in per unit area. On the other hand, HD increased with enlarging the intervals between the adjacent molten pools. Likewise for a large layer thickness, less laser energy for each particle was about to be allocated because more particles in per unit volume had to be heated, resulting in more un-melted particles with a higher occurrence of large localized pores and abnormal porosity.

 doi:10.20944/preprints202402.0218.v1

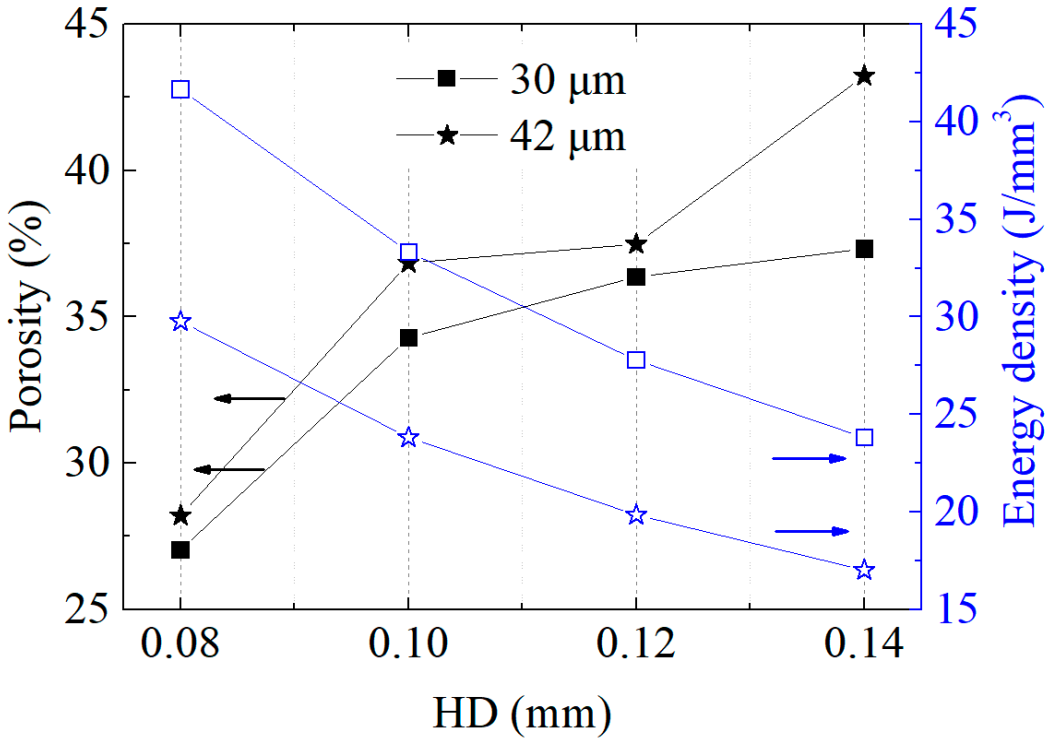

Figure 9. Porosity of microporous 316L fabricated by LPBF as a function of the different hatch distance at two layer thicknesses of 30 μm and 42 μm.

Correspondingly, the microstructure of microporous 316L samples fabricated with different HD at two LT of 30 μm and 42 μm was shown in Figure 10. All the pores displayed irregular-morphologies distributed homogenously along the molten tracks and the laser scanning routes (see further details in the magnifications). The distances between two adjacent molten tracks could be found in consistent with the set HD as used in the printing parameter, verified with the red dash marking lines in the magnifications in Figure 10a-d. With increasing the HD, the porous structures changed from the particle-stacking net porous structure with small-sized pores to that with large-sized interconnected ones, which illustrated that the pore structure can be arranged by the laser scanning route. Comparing the two LT samples, large LT meant less energy on per particle, making localized large pores more likely to appear, which was agree with the result of porosity.

 doi:10.20944/preprints202402.0218.v1

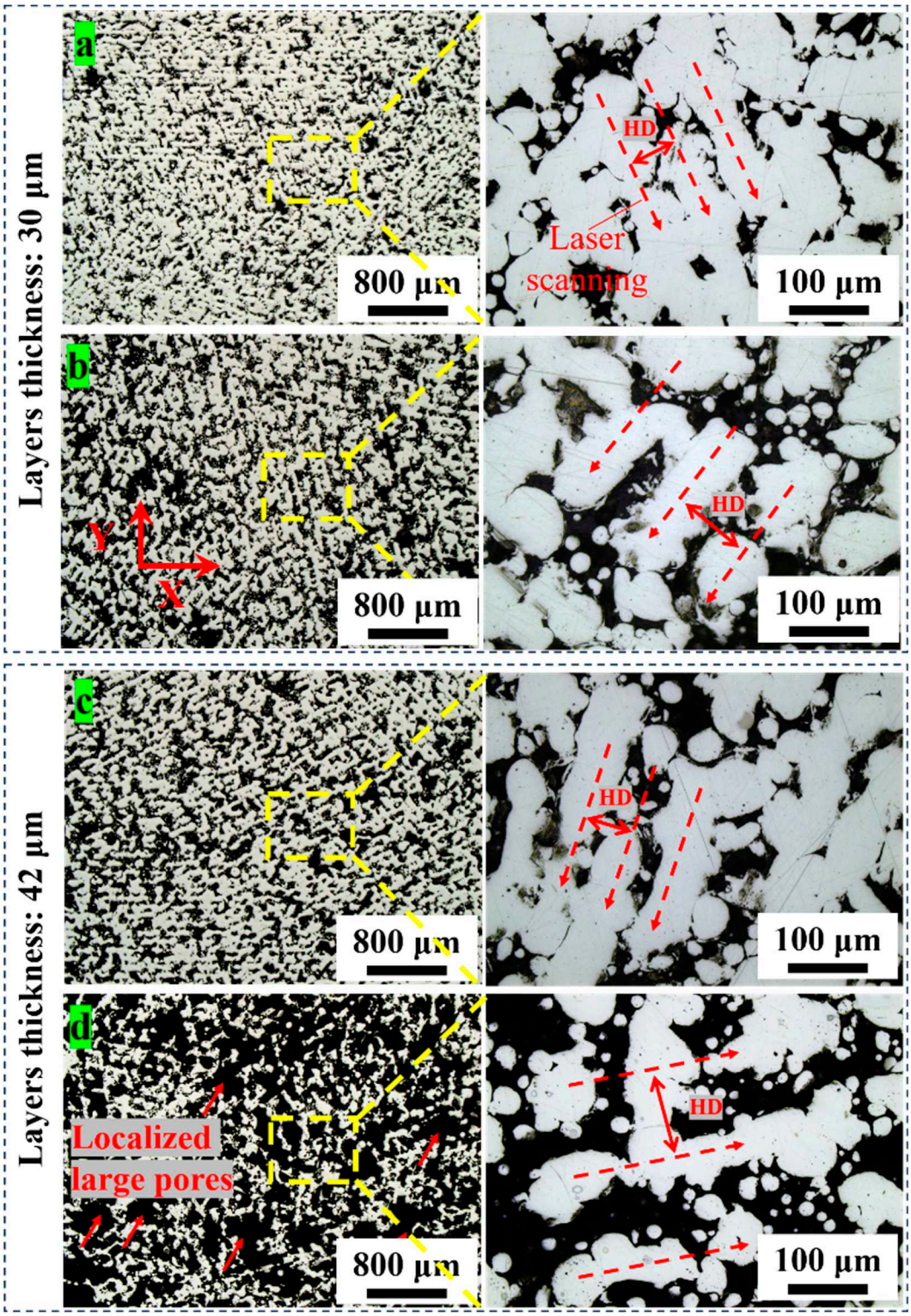

Figure 10. Cross-sectional pores of microporous 316L samples fabricated with different HD at two LT of 30 μm and 42 μm: (a) HD of 0.08 mm and (b) 0.14 mm at the LT of 30 μm, (c) HD of 0.08 mm and (d) 0.14 mm at the LT of 42 μm.

Table 3 shows the pore size of the samples fabricated with the HD of 0.08 mm and 0.14 mm and the LT of 30 μm and 42 μm. Figure 11 shows the corresponding pore size distribution. As the HD increased from 0.08 mm to 0.14 mm, the pore sizes of the samples printed with the LT of 30 μm increased 61.76% from 25.50 μm to 41.25 μm in D50 and 40.61% from 65.25 μm to 91.75 μm in D90. However, the samples printed with the LT of 42 μm showed only 21.19% increase from 37.75 μm to 45.75 μm in D50 but a large increment of 67.69% in D90, which demonstrated that less small-sized

 doi:10.20944/preprints202402.0218.v1

pores increased while more large-sized pores formed, that is, localized large pores, due to the increasing HD. As seen from the pore size distribution, it also showed a semi-gaussian distribution concentrated to left side. The difference is that it showed a lower percentage of small-sized pores below 10 μm, whereas there is a peak of size distribution between 10 μm to 100 μm.

Table 3. Pore size corresponding to the cross-sectional porous structure in Figure 10.

Sample		Mean(μm)	D50(μm)	D90(μm)	Porosity%
30 μm	0.08 mm	31.33	22.5	64.25	27.03
	0.14 mm	41.29	33.00	79.25	37.33
42 μm	0.08 mm	34.92	26.5	66.25	28.20
	0.14 mm	56.62	34.75	136.25	43.24

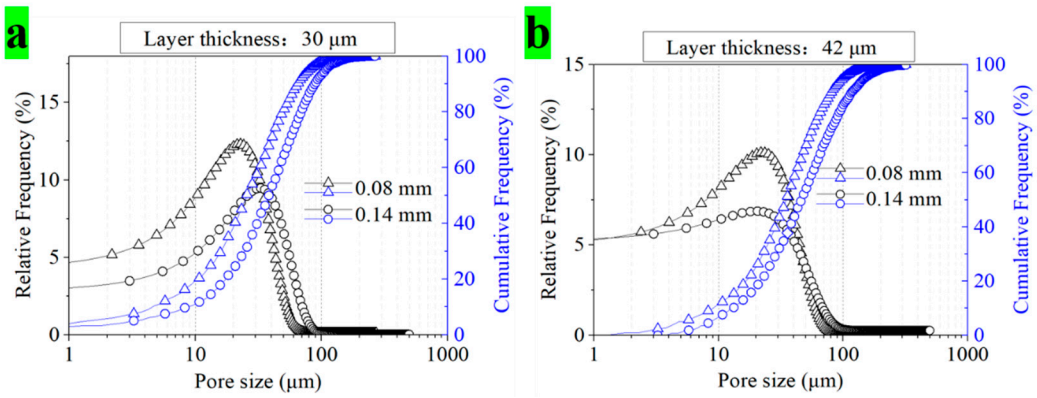

Figure 11. Pore size distribution of microporous 316L samples fabricated with different HD at two LT of 30 μm and 42 μm: (a) LT of 30 μm, (b) LT of 42 μm.

3.4. Three-Dimensional Pore Structure

In order to observe the overall pore structure, three-dimensional microstructure of microporous 316L was carried out by 3D X-Ray microscope, as shown with the computed tomography in Figure 12. As seen from the CT image, the sample as a whole formed a microporous structure with interconnected pores. The pores in XY plane (Figure 12b) evenly distributed along the direction of the laser scanning routes and mainly interconnected with each other along the molten tracks, while those in the planes (Figure 12c and d) of Z direction showed a relatively disordered distribution and mainly linked along the layered direction. Within the pores, lots of um-melted particles adsorbed on the struts. The struts formed by particle to particle overlapping in the molten tracks and layer textures could be clearly observed. Comparatively, Struts in XY direction dominated by laser scanning were more organized in comparison with that in Z direction determined by the layer thickness and laser impacting pressure, which indicated that pore distribution was more controllable in horizontal direction with controlling the laser scanning route and proper laser parameters.

 doi:10.20944/preprints202402.0218.v1

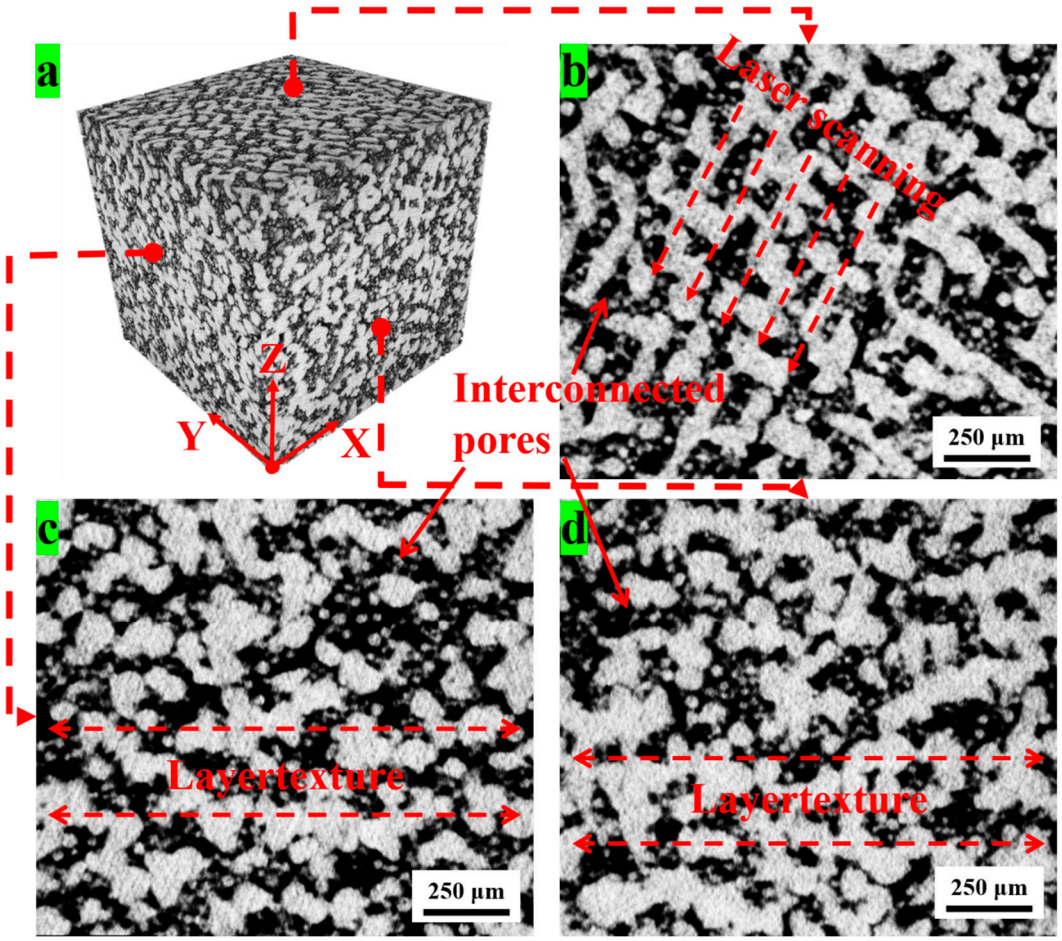

Figure 12. Three dimensional CT image of the of microporous 316L sample fabricated with an optimization of parameter: Power 60 w, Scanning speed 1000 mm·s^{-1}, HD 0.12 mm and LT 30 μm: (a) CT image of a 3x3x3 mm^3 microporous 316L cubic, (b) A cross-section in XY direction, (c) A cross-section in YZ direction (d) A cross-section in XZ direction.

3.5. Compressive Performance of Particle-Stacking Microporous 316L

The compressive performances of microporous 316L samples LPBF-fabricated with 600, 800, 1000 and 1200 mm·s^{-1} scanning speed and porous 316L prepared by the same LPBF-printing with lattice modeling as a comparison (i.e., lattice porous 316L) were undertaken. The stress-strain compressive curves were correspondingly plotted in Figure 13. All of the samples showed an elastic linear rising stage, a long period of inclined plastic yielding stage and a dramatic dropping stage, according with the compressive stress-strain curve of the typical porous metallic material [28,37,38]. This indicated that the pores in the structure can absorb part of loading energy before totally fractured. It also can be observed that the period of inclined plastic yielding stage and an energy-absorbing dropping stage of the sample with porosity of 28.02% was longer in comparison with other samples, indicating a longer plastic deformation and worse buffer effect because of its low porosity. With the increase of porosity, the compressive performances of the samples decreased with curves lying at significantly lower values, which was in agreement with the Ashby and Gibson model [39] on the relation between porosity and mechanical properties.

The compressive yield strengths of the particle-stacking microporous structure clearly decrease from 318.42 MPa to 79.44 MPa with the porosity ranging from 28.02% to 45.33%, which could be attributed to that large pores would generally yield ahead of the finer pores under the stress concentration. As the porosity increases, the amount and the thickness of wall struts acting as support skeletons in the architecture would reduce, in the meantime, generating lots of microcracks, where created local stress concentrations and served as locations of failure initiation upon mechanical loads

 doi:10.20944/preprints202402.0218.v1

in the end [41–43]. A comparison of the compressive yield strength of the lattice porous 316L with similar porosity of 29.05% was taken into account. It is interesting that that the yield strength (250.00 MPa) was 27.37% lower that of the particle-stacking microporous sample with porosity of 28.02%, showing a yield strength of 318.42 MPa. In particular, even the sample with higher porosity of 34.15% still showed a slightly higher yield strength (271.71 MPa) than that the 316L-lattice sample. These results indicated that microporous 316L fabricated by laser melting and stacking of particles possesses more advantages in the compressive performance. The particle-stacking microporous structure had more fine pores and a few localized large pores without systematic orientation and uneven pore surfaces, which better satisfied the conditions of the Ashby and Gibson model [39] and may contribute to a higher value of compressive strength. Conversely, the lattice porous structure had more homogenous and larger lattice-designed pores with systematic orientation might generate a detrimental effect on the mechanical property.

The corresponding deformation mode of the compressed samples underwent a different fracture morphology, from the typical shear fracture upon compression (i.e., the samples with porosity of 28.02% to 38.64%) to a destructive deformation of bulk integrated collapse (i.e., the sample with porosity of 45.33%), as shown Figure 13c, which illustrated an intergranular fracture feature [40]. It is worth noting that the porous 316L sample fabricated with lattice structure showed an integral bending deformation without fracture, indicating quite different mechanisms of the skeletons of particle-stacking porous and lattice porous under compression. The lattice porous 316L with a lower yield strength, however, still showed a compressed deformation of integral bending without generating any fractures, indicating a good toughness of lattice porous, which might relate to its more densified struts.

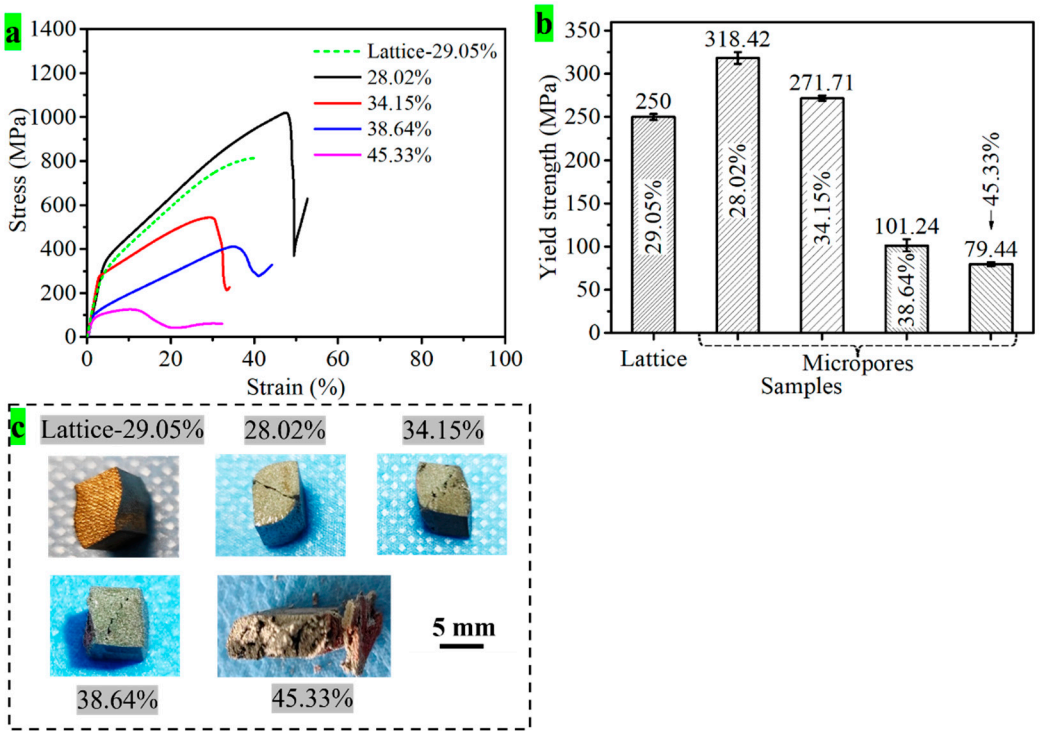

Figure 13. Compressive performances of the particle-stacking microporous 316L with different porosities, with a representative sample of lattice porous 316L as a comparison: (a) Representative stress-strain curves, (b) Morphologies of the fractured samples, (c) Yield strength.

4. Conclusions

316L with microporous structure was successfully fabricated by controlling the behaviors of melting and overlapping of 316L particles via using the characteristics of superfast heating and cooling of the laser energy. The main conclusions can be drawn as follows:

1. As a whole, the particle-stacking microporous 316L showed interconnected porous structure with homogenous pore distribution possessed a controllable normal porosity from 17.06% to 45.33%, pore size of D50 less than 50 μm and D90 less than 100 μm, and a high percentage of fine micropores distributed in the pore size of 1-10 μm. The pores in XY plane evenly distributed along the direction of the laser scanning routes and mainly interconnected with each other along the molten tracks, whereas the pore distribution in Z direction showed relatively disordered and mainly linked along the layered direction.
2. Laser energy density could not be taken as the determining indicator for the porosity and the formation of microporous structure. High-speed scanning mode showed a general effect on porosity variation, but it required a high laser power for the formation of porous structure, which might disorder the pore structure. Whereas, low-speed scanning would weaken the impact of laser energy pressure and the Marangoni flow on the stacking particles and formed the pores distributed along the laser scanning tracks with an organized pore structure. Narrow hatch distance could be contributed to stack a net porous structure with small pore size while wide hatch distance be beneficial for forming a particle-stacking porous structure with large-sized interconnected pores.
3. With the variation of porosity from 28.02% to 45.33%, the yield strength of microporous 316L varied from 318.42 MPa to 79.44 MPa. It showed a stronger compressive yield strength in comparison with the lattice porous 316L with the similar porosity.

Acknowledgements: The work was supported by the National Natural Science Foundation of China (Grant No.:52075421), the Guangdong Basic Applied Basic Research Foundation (Grant No.: 2020B1515130002) and the Ji Hua Laboratory Project (Grant No.: X202331TM200).

References

1. Balakrishnan Hari Kalathil, Doeven Egan H., Merenda Andrea, Dumée Ludovic F. & Guijt Rosanne M. (2021). 3D printing for the integration of porous materials into miniaturised fluidic devices: A review. Analytica Chimica Acta 338796-338796. https://doi.org/10.1016/J.ACA.2021.338796.
2. Junhua Qin, Qing Chen, Chunyan Yang & Yong Huang. (2016). Research process on property and application of metal porous materials. Journal of Alloys and Compounds 39-44. https://doi.org/10.1016/j.jallcom.2015.09.148.
3. Wen Lei, Nie Meng, Wang Chongqing, Zhao Yuna, Yin Kuibo & Sun Litao. (2021). Multifunctional, Light-Weight Wearable Sensor Based on 3D Porous Polyurethane Sponge Coated with MXene and Carbon Nanotubes Composites. Advanced Materials Interfaces (5). https://doi.org/10.1002/ADMI.202270027.
4. Fu Chong, Liang Jianwei, Yang Gao, Dagestani Abd alwahed, Liu Wei, Luo Xudong, Zeng Baobao, Wu Haidong, Huang Meipeng, Lin Lifu, Deng Xin. Recycling of waste glass as raw materials for the preparation of self-cleaning, light-weight and high-strength porous ceramics[J]. Journal of Cleaner Production, 2021, 317. https://doi.org/10.1016/J.JCLEPRO.2021.128395.
5. ResendeGonçalves Cláudia Inês, Sampaio Nuno, Moreira Joaquim, Carvalho Oscar, Caramês João, ManzanaresCéspedes Maria Cristina.&Souza Júlio. (2022). Porous Zirconia Blocks for Bone Repair: An Integrative Review on Biological and Mechanical Outcomes. Ceramics (1), 161-172. https://doi.org/10.3390/CERAMICS5010014.
6. Germaini Marie-Michèle, Belhabib Sofiane, Guessasma Sofiane, Deterre Rémi, Corre Pierre, Weiss Pierre. Additive manufacturing of biomaterials for bone tissue engineering – A critical review of the state of the art and new concepts[J]. Progress in Materials Science, 2022, 130. https://doi.org/10.1016/J.PMATSCI.2022.100963.
7. Kelly Cambre N., Wang Tian, Crowley James, Wills Dan, Pelletier Matthew H., Westrick Edward R., Adams Samuel B., Gall Ken, Walsh William R. High-strength, porous additively manufactured implants with optimized mechanical osseointegration[J]. Biomaterials, 2021, 279 121206-121206. https://doi.org/10.1016/J.BIOMATERIALS.2021.121206.
8. Abdelgawad Khaled Z., Adebayo Abdulrauf R., Isah Abubakar, Muhammed Nasiru S. A literature review of strength and stability of foam and their relationship with the absolute permeability of porous media[J]. Journal of Petroleum Science and Engineering, 2022, 211. https://doi.org/10.1016/J.PETROL.2022.110195.

9. Yuksel C. Yabansu, Patrick Altschuh, Johannes Hötzer, Michael Selzer, Britta Nestler, Surya R. Kalidindi. A digital workflow for learning the reduced-order structure-property linkages for permeability of porous membranes[J]. Acta Materialia, 2020, 195 (prepublish): 668-680. https://doi.org/10.1016/j.actamat.2020.06.003.
10. Xiaocui Yang, Xinmin Shen, Haiqin Duan, Xiaonan Zhang, Qin Yin. Identification of Acoustic Characteristic Parameters and Improvement of Sound Absorption Performance for Porous Metal[J]. Metals, 2020, 10 (3): 340-340. https://doi.org/10.3390/met10030340.
11. Sun Wenhao, Pan Baorui, Song Xiang, Xiao Heye, Zhou Jie, Sui Dan. A novel sound absorber design of nanofibrous composite porous material[J]. Materials & Design, 2022, (prepublish): 110418-. https://doi.org/10.1016/J.MATDES.2022.110418.
12. X. B. Xu, P. S. Liu, G. F. Chen, C. P. Li. Sound Absorption Performance of Highly Porous Stainless Steel Foam with Reticular Structure[J]. Metals and Materials International, 2020, 27 (9): 1-9. https://doi.org/10.1007/s12540-020-00701-0.
13. G Trilok, Srinivas Kurma Eshwar Sai, Harikrishnan Devika, N Gnanasekaran, Mobedi Moghtada. Correlations and Numerical Modeling of Stacked Woven Wire-Mesh Porous Media for Heat Exchange Applications[J]. Energies, 2022, 15 (7): 2371-2371. https://doi.org/10.3390/EN15072371.
14. Wyczółkowski Rafał, Bagdasaryan Vazgen, Gała Marek, Król Paweł Artur. The Review of Chosen Methods Used to Investigate Heat Transfer in a Steel Porous Charge[J]. Energies, 2022, 15 (6): 2266-2266. https://doi.org/10.3390/EN15062266.
15. Liang Xiong, Li Yawei, He Zhu, Yan Wen, Tan Fangguan, Wang Qinghu, Zhu Tianbin, Sang Shaobai. The effect of cellular structure on the strength and combustion properties of SiC porous ceramics[J]. Ceramics International, 2022, 48 (2): 2538-2545. https://doi.org/10.1016/J.CERAMINT.2021.10.036.
16. Tao Xuefeng, Yang Zhao, Cheng Menghao, Yan Rui, Chen Fan, Cao Sujiao, Li Shuang, Ma Tian, Cheng Chong, Yang Wei. Phosphorus modulated porous CeO2 nanocrystallines for accelerated polysulfide catalysis in advanced Li-S batteries[J]. Journal of Materials Science & Technology, 2022, 131 212-220. https://doi.org/
17. Lu Wenjing, Li Tianyu, Yuan Chenguang, Zhang Huamin, Li Xianfeng. Advanced porous composite membrane with ability to regulate zinc deposition enables dendrite-free and high-areal capacity zinc-based flow battery[J]. Energy Storage Materials, 2022, 47 415-423. https://doi.org/10.1016/J.ENSM.2022.02.034.
18. Federico M ,Elisa E ,Maxime H , et al. Electrode kinetics of porous Ni-3YSZ cermet operated in fuel cell and electrolysis modes for solid oxide cell application [J]. Electrochimica Acta, 2021, 389. https://doi.org/10.1016/J.ELECTACTA.2021.138765.
19. Ibrahim Mohd Hakim, Mustaffar Mohd Idham, Ismail Syarifah Aminah, Ismail Anis Nadhirah. A Review of Porous Glass-Ceramic Production Process, Properties and Applications[J]. Journal of Physics: Conference Series, 2022, 2169 (1). https://doi.org/10.1088/1742-6596/2169/1/012042.
20. Shweta Singh, Naresh Bhatnagar. A survey of fabrication and application of metallic foams (1925–2017)[J]. Journal of Porous Materials, 2018, 25 (2): 537-554. https://doi.org/10.1007/s10934-017-0467-1.
21. John Banhart. Manufacture, characterisation and application of cellular metals and metal foams[J]. Progress in Materials Science, 2001, 46 (6): 559-632. https://doi.org/10.1016/S0079-6425(00)00002-5.
22. Pfeiffer Stefan, Florio Kevin, Puccio Dario, Grasso Marco, Colosimo Bianca Maria, Aneziris Christos G., Wegener Konrad, Graule Thomas. Direct laser additive manufacturing of high performance oxide ceramics: A state-of-the-art review[J]. Journal of the European Ceramic Society, 2021, 41 (13): 6087-6114. https://doi.org/ 10.1016/J.JEURCERAMSOC.2021.05.035.
23. J. Gunasekaran, P. Sevvel, I. John Solomon. Metallic materials fabrication by selective laser melting: A review[J]. Materials Today: Proceedings, 2020, (prepublish). https://doi.org/10.1016/j.matpr.2020.05.162.
24. Dhiman S ,Sidhu S ,Bains S P , et al. Mechanobiological assessment of Ti-6Al-4V fabricated via selective laser melting technique: a review [J]. Rapid Prototyping Journal, 2019, 25 (7): 1266-1284. https://doi.org/10.1108/RPJ-03-2019-0057.
25. Chunze Yan, Liang Hao, Ahmed Hussein, Philippe Young, David Raymont. Advanced lightweight 316L stainless steel cellular lattice structures fabricated via selective laser melting[J]. Materials & Design, 2014, 55 533-541. https://doi.org/10.1016/j.matdes.2013.10.027.
26. Prajapati, Mayur & Kumar, Ajeet & Jeng, Jeng-Ywan. (2022). Multi-material additive manufacturing with lightweight closed-cell foam-filled lattice structures for enhanced mechanical and functional properties. Additive Manufacturing. 54. 102766. https://doi.org/10.1016/j.addma.2022.102766.

27. Tianlin Zhong, Ketai He, Huaixue Li, Lechang Yang. Mechanical properties of lightweight 316L stainless steel lattice structures fabricated by selective laser melting[J]. Materials & Design, 2019, 181 108076-108076. https://doi.org/10.1016/j.matdes.2019.108076.
28. Jinguo Ge, Jian Huang, Yongping Lei, Peter O'Reilly, Mansur Ahmed, Chao Zhang, Xingchen Yan, Shuo Yin. Microstructural features and compressive properties of SLM Ti6Al4V lattice structures[J]. Surface & Coatings Technology, 2020, 403 126419-. https://doi.org/10.1016/j.surfcoat.2020.126419.
29. Li Zhenjun, Takano Naoki, Mizutani Masayoshi. Material properties of selective laser melting additive-manufactured Ti6Al4V alloys with different porosities[J]. Precision Engineering, 2023, 83 142-151. https://doi.org/10.1016/j.matdes.2020.109035.
30. Lin Ting-Chiang, Cao Chezheng, Sokoluk Maximilian. & Li Xiaochun. Aluminum with dispersed nanoparticles by laser additive manufacturing. [J]. Nature communications, 2019, 10 (1): 4124. https://doi.org/10.1038/s41467-019-12047-2.
31. Won Rae Kim, Gyung Bae Bang, Ohyung Kwon, Kyung-Hwan Jung, Hyung-Ki Park, Gun-Hee Kim. & Hyung Giun Kim. (2020). Fabrication of porous pure titanium via selective laser melting under low-energy-density process conditions. Materials & Design (prepublish), 109035-. https://doi.org/10.1016/J.PRECISIONENG.2023.06.006.
32. Bruce Duncan W., O'Hare Dermot, Walton Richard I. Porous Materials[M]. John Wiley & Sons, Ltd: 2010-10-19. https://doi.org/10.1002/9780470711385.
33. E. Sallica-Levaa, A.L.Jardinib, J.B.Fogagnoloa. Microstructure and mechanical behavior of porous Ti–6Al–4V parts obtained by selective laser melting[J]. Journal of the Mechanical Behavior of Biomedical Materials, 2013, 26 98-108. https://doi.org/10.1016/j.jmbbm.2013.05.011.
34. Saad A. Khairallah, Andrew T. Anderson, Alexander Rubenchik, Wayne E. King. Laser powder-bed fusion additive manufacturing: Physics of complex melt flow and formation mechanisms of pores, spatter, and denudation zones[J]. Acta Materialia, 2016, 108 36-45. https://doi.org/10.1016/j.actamat.2016.02.014.
35. Meier Christoph, Penny Ryan W., Zou Yu, Gibbs Jonathan S. & Hart A. John.(2017). Thermophysical phenomena in metal additive manufacturing through selective laser melting: fundamentals, modeling, simulation, and experimentation [J]. Annual Review of Heat Transfer, 2017, 20 (1): 241-316. https://doi.org/10.1615/ANNUALREVHEATTRANSFER.2018019042.
36. Hailong Liao, Junjie Zhu, Shijie Chang, Gang Xue, Haihong Zhu, Baijin Chen. Al2O3 loss prediction model of selective laser melting Al2O3–Al composite[J]. Ceramics International, 2020, 46 (9): 13414-13423. https://doi.org/10.1016/j.ceramint.2020.02.124.
37. Chen Xu, Wu Yanlong, Liu Huilong, Wang Yaning, Zhao Guangbin, Zhang Qingxian, Wang Fu, Liu Yaxiong. Mechanical performance of PEEK-Ti6Al4V interpenetrating phase composites fabricated by powder bed fusion and vacuum infiltration targeting large and load-bearing implants[J]. Materials & Design, 2022, (prepublish): 110531-. https://doi.org/10.1016/J.MATDES.2022.110531.
38. Liu Jiangwei, Guo Kai, Sun Jie, Sun Qidong, Wang Leishuo, Li Hu. Compressive behavior and vibration-damping properties of porous Ti-6Al-4V alloy manufactured by laser powder bed fusion[J]. Journal of Manufacturing Processes, 2021, 66 1-10. https://doi.org/10.1016/J.JMAPRO.2021.03.060.
39. Gibson, L.J., Ashby, M.F., 1997. Cellular Solids-Structure and Properties, seconded. Cambridge university, Cambridge.
40. Zhou Kai, Chen Wenge, Yang Yana, Li Rong, Dong Longlong, Fu Yong Qing. Microstructure and mechanical behavior of porous tungsten skeletons synthesized by selected laser melting[J]. International Journal of Refractory Metals and Hard Materials, 2021, (prepublish): 105769-. https://doi.org/10.1016/J.IJRMHM.2021.105769.
41. Zhou Kai, Chen Wenge, Yang Yana, Li Rong, Dong Longlong, Fu Yong Qing. Microstructure and mechanical behavior of porous tungsten skeletons synthesized by selected laser melting[J]. International Journal of Refractory Metals and Hard Materials, 2021, (prepublish): 105769-. https://doi.org/10.1016/J.IJRMHM.2021.
42. E. Sallica-Leva, A.L. Jardini, J.B. Fogagnolo. Microstructure and mechanical behavior of porous Ti–6Al–4V parts obtained by selective laser melting[J]. Journal of the Mechanical Behavior of Biomedical Materials, 2013, 26 98-108. https://doi.org/10.1016/j.jmbbm.2013.05.011.
43. Andrey Vyatskikh, Stéphane Delalande, Akira Kudo, Xuan Zhang, Carlos M. Portela1 & Julia R. Greer. Additive manufacturing of 3D nano-architected metals. [J]. Nature communications, 2018, 9 (1): 593. https://doi.org/10.1038/s41467-018-03071-9.

 doi:10.20944/preprints202402.0218.v1